Deposit shape control for local repair and welding by cold spray

Amir Ardeshiri Lordejani, Luca Romanenghi, Andrea Pollastri, Mario Guagliano, Sara Bagherifard *

Politecnico di Milano, Department of Mechanical Engineering, Milan, Italy

A R T I C L E I N F O	A B S T R A C T

Cold spray (CS) has proven to be a versatile deposition method with considerable capabilities in multiple fields including coating, additive manufacturing, and repair. Despite the significant progress in new applications of cold spray, there are still several challenges associated with controlling the shape of cold spray deposits that consequently affect their range of application and functionality. In this study, we discuss and demonstrate a new application of CS to connect adjoining edges along with repair local damages, focusing on deposit shape prediction. To do so, we start by proposing a numerical model that can predict the CS deposit geometry, by providing specific input parameters for a given set of particle and substrate properties, substrate geometry and nozzle position. Then we employ this numerical method to design the toolpath required for filling the artificial local damages and/or the welding grooves with controlled geometries. Through comparing the predictions with the shape of experimentally obtained depositions, we propose some corrections for the model. In both local repair and welding cases, the experimental results show a great resemblance to the predicted deposit profile and after applying the corrective measures, to the deposit height.

1. Introduction

In cold spray (CS) method, particles' high kinetic energy, arising from their high velocity, is the main contributor to the adhesion phenomenon. Hence, in contrast to other thermal spraying methods, CS does not require high gas temperature, making it less prone to undesirable characteristics such as recrystallization and extensive oxidation [1]. Hence CS allows for additive manufacturing (AM) deposition of oxygen-sensitive, temperature sensitive, and highly reflective materials [2]. Furthermore, in comparison to other AM methods, CS can achieve a very high deposition rate and thus has higher buildup rate [3,4]. These advantages along with the possibility of working with dissimilar material systems [5], make CS a compelling solution for repair of local damages as well as welding different joint configurations [6].

When considering methods of joining metallic parts, conventional welding procedures would be the initial widespread options. However, those methods inevitably involve the melting and re-solidification of either a filling material or the adjoining edges of the involved parts themselves. In either case, the welding requires a considerable energy input, mostly in the form of thermal energy, which will lead to changes in the material microstructure, and may cause the formation of microcracks at the vicinity of welding region. The material at the zone between the weld and the base unaffected material, referred to as the Heat Affected Zone (HAZ), experiences severe thermal changes. The relevant temperature variation will result in change of grain size, crystalline structure, and arrangement, and eventually mechanical properties of the HAZ. Furthermore, the thermal input of the welding process followed by the solidification phase may result in distortion, undesired residual stresses, formation of hot cracks due to the presence of impurities, and cold cracks arising from rapid cooling or hydrogen absorbed by the molten pool [7,8]. The aforementioned issues can be mitigated using conventional methods such as pre-heating or post-weld heat treatment [9] or novel methods such as the use of weld fillers with low transformation temperatures [10], all of which increase the overall cost and time and thus limit the application scope of the welding methods.

In addition to thermal parameters, the quality of welding and the joint's mechanical characteristics depend on the joint type, welding position, and base metal thickness. Many studies have discussed and demonstrated the effect of weld seam geometry on the weld fillet geometry, and their consequent influence on properties such as fatigue life of the weld [11]. This calls for a careful selection of the weld seam geometry.

On the other hand, similar set of challenges exist for conventional methods of repair and remanufacturing, where in addition to restoration

---

* Corresponding author.
E-mail address: sara.bagherifard@polimi.it (S. Bagherifard).

of the original geometry, the performance of the restored section should be recovered to be the same as the pristine part if not better. Some of these methods include brazing [12], Tig welding [13], laser engineered net shaping [14,15], direct energy deposition [16–18], etc. It should be noted that repair methods generally may require surface preparation and extension of the damage geometry to a controlled form, as well as thermo-mechanical pre- and post-processes.

When considering the characteristics of CS, it seems to satisfy numerous requirements of a repair and joining method, while avoiding many of the above-mentioned critical shortcomings of current processes. However, its application for these purposes demands a high control over the deposit shape. Hence, a method to predict the geometry of deposited material will be essential. There have been previous attempts at developing numerical models to simulate the deposition process and the final geometry of the coating. Observations suggest that the final geometry depends on combination of substrate-coating material, spraying parameters such as gas temperature and pressure, stand-off distance, nozzle traverse speed, nozzle inclination, and the spatial arrangement of tracks.

Klinkov et al. [19] developed a model, which predicts the cumulative deposit profile for a series of parallel tracks based on the substrate geometry, relative placement of the spraying tracks, and the variation of deposit height across transverse cross section of a single track. Their model attempts to predict the deposit height at any given point across the transverse cross-section as a function of its coordinate across the single-track width, angle of spray, and time. The track profile approximates the observed CS deposit cross-section geometry resulting from one straight pass for a set of powder-substrate material and spray parameters combination. Later, they introduced a generalized definition of nozzle-substrate angle [20]. By employing this new parameter in a modified definition of deposition efficiency (DE), along with and definition of particle jet distribution parameter, they proposed a formula to predict the deposit profile growth in 3D. The model is described in detail in Section 2.

Wu et al. considered the formation of CS deposits on non-flat substrate surfaces. They employed a thickness growth function similar to one proposed by Klinkov et al. [20]. But their model relies on dividing the sprayed powder beam into rays that originate from nozzle outlet and diverge until they reach the deposit radius at intersection with the substrate. Then from intersection point of each ray on the substrate, a cylinder is raised along that ray. Each cylinder has a diameter of 0.02 mm and a height that corresponds to the value of Gaussian deposit growth function at that point. Consideration of non-flat substrate surfaces led to the proposal of the shadow effect [21]. Shadow effect refers to the situation where the powder trajectory coincides with more than one section of the substrate surface, therefore the most proximate section prevents the powder flow from reaching, impacting, and probably depositing on the subsequent surfaces beneath it.

In an attempt to further increase the application of CS as an AM method, Vanerio et al. [22] proposed an enhanced model capable of predicting more free-form deposits. To do so, they based the model on the one proposed by Klinkov et al. [20], but developed it to include the effect of wide-range nozzle inclination, shadow effect, deposit profile shape for materials with non-gaussian track profiles, its development on non-planar substrates, and the generation of superimposed tracks in 3D. The model was then validated against an extensive range of experiments, confirming the high accuracy and flexibility of the developed model.

Along with the growing interest in this topic, some researchers such as Ikeuchi et al. have started to incorporate novel methods like "artificial neural network" (ANN) as a predictive model for geometric control of CS deposits [23]. They demonstrated the capability of their model to predict the effect of nozzle angle, transverse speed, stand-off distance, and its application for online programming of the robot-actuated motion of the nozzle to achieve a desired final profile. However, as it is inherent to the nature of an ANN algorithms, the quality of the results relies heavily

on the existence of a massive library of experimental data for training the algorithm.

In this research, we developed a numerical model based on a previous study in our group [22]. The presented numerical model can predict the amount of deposited powder and its spatial distribution on the substrate, depending on nozzle's placement. The deposit geometry depends on the volumetric distribution of the outcoming powder with respect to the nozzle axis, the powder impact angle, and the duration of time nozzle spends at any given coordinate, expressed as nozzle's traverses speed and number of passes over each track. The model was used to accurately predict the geometry of cold sprayed deposits for repairing superficial cavities with various geometries and welding joints with different inclinations.

The target of these simulations was to achieve a good deposit shape with a feasible trajectory, to potentially reduce the post-process machining steps. At this stage of our study, other factors, such as minimizing the powder waste, while noteworthy, were not targeted.

In the following sections, first, the numerical model for simulation of deposit growth is described. Then the experiments are described and categorized in two series; the first series of experiments are conducted for obtaining input parameters required to set up the predictive model, while the second series of experiments are focused on replicating the welding and repair configurations derived from the simulations. The results are then compared to evaluate the accuracy of the numerical model. This analysis leads to the definition of a correction factor for the numerical model based on a few intrinsic complications and simplifying assumptions that will be discussed. Finally, the corrected results are compared, and the applications and further possible enhancements of the numerical model are discussed.

2. Method and materials

2.1. Numerical model

2.1.1. Deposit growth simulation

The intended function of this numerical model is to predict the CS deposit profile of a specific powder on a substrate of arbitrary material and shape, with a given set of primary (e.g., Carrier gas stagnation pressure and temperature, particle size distribution, etc.) and secondary (e.g., nozzle's traverse speed, stand-off distance, etc.) parameters with any desired scanning strategy.

The model consists of a series of scripts implemented in MATLAB, based on the mathematical, time-dependent model proposed by Klinkov et al. [20], further developed by Vanerio et al. [22]. Klinkov's model assumes that for a given position of nozzle with respect to the substrate, the deposit profile height at each point depends on

- the volumetric distribution of the outcoming powder with respect to the nozzle axis,
- the powder impact angle, and
- the duration of time the nozzle spends at any given coordinate.

First, substrate's coordinate system should be defined, where the xy plane lies on the substrate surface with the x axis directed along the nozzle's trajectory, making the z axis normal to the substrate plane.

Powder impact angle, α, can be defined as the angle between the target surface – which will be substrate surface during the first pass or deposit's plane during consequent passes – and the plane perpendicular to the nozzle axis. To define α in 3D, 2 vectors need to be defined, the normal vector of the deposit's plane and the nozzle's axis vector. Normal vector of the deposit's plane can be defined using its angle with respect to substrate plane at each point $\left(\gamma_x, \gamma_y, 0\right)$. Knowing this, the deposit's plane normal vector can be expressed by the deposit profile's gradient as $v_n = \left[tan\gamma_x, tan\gamma_y, 1\right]$, and consequently by profile derivative $v_c =$

$\left[-\frac{\partial z}{\partial x}, -\frac{\partial z}{\partial y}, 1\right]$. Meanwhile, the nozzle's axis vector can be described using its tilt angles with respect to the substrate $\left(\beta_x, \beta_y\right)$ as $\left[tan\beta_x, tan\beta_y, 1\right]$. Therefore, the impact angle will be calculated as Eq. (1):

$$tan(\alpha) = \frac{\|\overline{v_c} \times \overline{v_n}\|}{\overline{v_c} \cdot \overline{v_n}} \tag{1}$$

This model assumes an initially flat substrate and proposes that DE is primarily a function of the powder impact angle. This correlation is proposed for 3D model in the form of Eq. (2):

$$\text{DE}(tan(\alpha)) = \begin{cases} \dfrac{e^{-k\left(\frac{tan(\alpha)}{tan(\alpha_m)}\right)^2} - e^{-k}}{1 - e^{-k}} & tan(\alpha) < tan(\alpha_m) \\ 0 & \text{otherwise} \end{cases} \tag{2}$$

where $k = 4.5$, and $tan(\alpha_m) = 1.2$ that corresponds to a maximum impact angle of $\alpha_m = 50°$ for successful particle adhesion. These constants are reported by the Klinkov et al. [20] and have been extracted from the experimental data of cold sprayed Cu and Al powders.

Klinkov et al. proposed an axisymmetric, gaussian-based approximation for the distribution profile of powder flow, introducing it as volumetric specific feed rate $J(r)$ as expressed in Eq. 3; this assumption implies that the distribution depends only on the distance of the target point from the nozzle axis (r).

$$J(r) = \begin{cases} \dfrac{e^{-k_2(r/r_n)^2} - e^{-k_2}}{1 - e^{-k_2}} & r < r_n \\ 0 & \text{otherwise} \end{cases} \tag{3}$$

r_n and k_2 are fitting parameters that depend on the width of single-track profile and its inclination at the boundaries. r is the distance between a generic point on the deposit and the nozzle's axis.

Klinkov et al. [20] assumed the deposit's growth to be along the z direction, regardless of the nozzle's inclination. Thus, it is necessary to transform the powder volume passing through a portion of the jet's cross section to the volume being deposited on the corresponding coating target area, and consequently on the corresponding substrate area. This can be done by sequential projection of areas based on the angles between the nozzle and the deposit surface and that between the deposit surface and the substrate surface.

By substituting these equations into the formula proposed for the deposit growth rate, the following partial differential equation (PDE) will be achieved.

$$\frac{\partial z_{axis}}{\partial t} = A \bullet \text{DE}(tan(\alpha)) \bullet J(r) \tag{4}$$

This equation is first discretized using method of lines [24]; then boundary and initial conditions taken from the basic experiments are used to determine the value of the constants and coefficients. Time is discretized with appropriately chosen step values. Since the final equation is an ordinary differential equation (ODE), a simple predictor-corrector method (following Heun's method [25]) is used to first approximate the slope of the function at a specific time interval (using Euler's method), and then to increase the accuracy of the estimated value (using trapezoidal rule).

2.1.2. Modifications with respect to the original model

Vanerio et al. [22] generalized this model by assuming the particle jet distribution being still axisymmetric, but not necessarily with a Gaussian form. In addition, the limitation of initially flat substrate was relaxed, offering the possibility to consider a freeform substrate. The substrate geometry CAD file can be defined in stereolithography (STL) format, discretized into well-refined triangular elements. Each element was represented by its normal vector and coordinates of its three vertices. This independence from a fixed coordinate system also allows the assumption of a non-straight nozzle trajectory. Having the nozzle trajectory and the STL of substrate offers the flexibility to calculate the deposit growth for each triangular face along the direction of nozzle, and not only along the z-axis.

The updated model also considered the effect of spray distance, d_s, (aka.stand − off distance, by introducing a new deposition efficiency term that depends on stand-off distance ($\text{DE}_d(d_s)$) and considering d_s as a new variable in the jet's particle distribution profile ($J(r, d_s)$). The values for these two additional variables should be extracted from experimental data.

Finally, the shadow effect, that is the obstructive effect of some faces of the substrate or already-formed deposit on the powder flow and deposition on the covered sections behind them, was also considered. To do so, the powder flow was assimilated to parallel rays initiating from the nozzle's outlet. Then the intersection points of these rays with all the faces was identified, and the deposit growth was simulated only on the face closest to the nozzle outlet.

2.1.3. Required inputs for the numerical model

This model allows for considering shadow effect, dynamic remeshing, capability of accepting any 3D STL file as the substrate geometry, simulation of deposit growth parallel to the nozzle direction, extending dependency of deposition efficiency to stand-off distance in addition to angle of impact, and flexibility in simulating the resultant deposit for any nozzle trajectory. Furthermore, this model offers the possibility to assume a non-gaussian powder jet material distribution, which has been observed for some powder materials. The mentioned enhancements allow for implementation of any desired substrate geometry and toolpath trajectory and make it possible to predict the deposit geometry and final profile for a wide variety of material combinations and different applications, efficiently and accurately. This makes the results more reliable and makes the code suitable for a wider variety of sprayed materials. However, each aspect of the model relies on the knowledge of specific parameters for CS deposits of a specific material system (powder and substrate materials combination), and parameters, which define the desired motion of nozzle with respect to the substrate. The first set of parameters are determined as described here, and the second set of parameters are achieved by iterative optimization of their initial proposed values.

Implementation of this numerical model requires the knowledge of deposit's cross-section profile for a specific pair of substrate-powder materials and various nozzle angles, stand-off distances, and nozzle traverse speeds. DE functions $\text{DE}(tan(\alpha))$ and $\text{DE}_d(ds)$ can be acquired by fitting a curve to the mapped experimental values of DE for a variety of nozzle angles and stand-off distances, respectively. $\text{DE}(tan\alpha)$ is approximated with the proposed modified form of the Gaussian function, and $\text{DE}(d)$ is expressed as a fourth order polynomial function. The width and steepness angle at the lateral ends of acquired profiles for single tracks sprayed at $90°$ with constant primary parameters, varying only d_s, together with consideration of constant mass are used as the input for fitting the modified Gaussian powder distribution $J(r, d_s)$. The single-track profiles with same sets of parameters and variable numbers of passes are used to determine coating growth speed at the center of track A (mm/s). This data will help solve the PDE for deposit growth estimation.

The determined deposit thickness growth equation, together with the parameters that describe the motion of nozzle including initial and final point coordinates x_i, x_f, spray angle β_y, stand-off distance d_s, transverse speed v_t, time step t_{step} and number of passes n_p will help estimating the deposit profile after a specific motion. A script was developed to automatically calculate the nozzle position vector $\overrightarrow{v}_{nposition}$, the nozzle axis vector $\overrightarrow{v}_n$, and the time vector $\overrightarrow{t}$.

Another modification implemented in the model, As presented by Vanerio et al. [22], is individual consideration of the powder impact

angle and deposition growth for each triangular face, through which powder stream is passing. Hence, simulation results will be more accurate compared to other methods.

The developed model was initially validated by simulating and comparing the predicted and reported results of three cases for which the required input data and the coating profile were available in the literature [22,26]. The cases involve deposition of Ti6Al4V powder on two tracks with different nozzle inclinations on a flat substrate, a single track on a curved substrate, and spraying on a substrate with complex geometry to evaluate the shadow effect. In all three cases, our model's predicted deposit profiles were closely aligned with the experimental results.

2.1.4. Determination of the optimized nozzle toolpath

The current model is developed to accommodate any complicated substrate geometry in 3D, based on its stereolithography (STL) file. For cases considered in this research, we assumed the nozzle traverse speed to be constant and all optimized toolpaths to consist of parallel tracks along the X-axis (along the length of the cavity slot and welding edge). Moreover, it is assumed that in all cases, the excess material of the final CS deposit will be machined to achieve a flat surface.

The optimized toolpath strategy is determined through an iterative approach demonstrated in Fig. 1. The first step is to decide whether to start with a central track or to fill in the corners before proceeding with the other tracks. After establishing the arrangement of the first track (or two initial corner tracks) the general cycle begins. Each iteration cycle starts with the definition of a track's deposition parameters (nozzle axis position, nozzle angle, number of passes, etc.) and is followed by simulation of the resultant deposit. If the achieved deposit is satisfactory, the next iteration of the cycle will start with definition of the track's placement and the parameters for the next track. Otherwise, track parameters will be individually modified in a sequential manner until the deposit quality criteria (e.g., relative flatness or appropriate condition for placement of the next track) are satisfied, at which point the cycle will restart with parameter definition of the next track. In either case, before definition of a new track, three main criteria are controlled, and if all are satisfied, the cycle will be terminated. The first criterion is symmetry of the deposit with respect to longitudinal plane of symmetry of cavity or the butt joint. The second criterion is verification of a minimum overall flatness of the surface, which is determined in terms of the height difference between the lowest and highest point of the deposit profile inside the repair or welding region. A 0.5 mm threshold is set for the maximum allowable height difference. The third is that the deposit should protrude the cavity (both in the case of welding and filling the local defect) so that after machining the excess material, a flat surface can be achieved.

It should be noted that the kinematic parameters were selected considering the constraints of the available cold spray gun and the robotic arm as its maneuvering device. These include robotic arm's range of motion, collision evasion, as well as general CS deposition requirements like the necessity for a direct line of sight.

2.2. Experimental tests

2.2.1. Material and methods

Having a widespread use in industry, stainless steel AISI S316L was selected both for the substrate and powder feedstock, with the nominal chemical composition as reported in Table 1.

Spherical 316L powder (Metalpine GmbH, AT) with $D10 = 16.62\ \mu m$, $D50 = 27.16\ \mu m$, and $D90 = 42.35\ \mu m$ and apparent density of $4.77\ g/cm^3$ was used as the feedstock. Size distribution and the sphericity of the powder were assessed with Malvern Mastersizer 2000E (Malvern Instruments Ltd., Worcestershire, UK) and through SEM imaging, respectively. The results indicated notable sphericity with an aspect ratio of 0.98 ± 0.178, as confirmed by Fig. 2.

All the substrates were cut from the same 5 mm thick rolled S316L sheet and then slots, cavities, or edge shape, as described in the next section, were made using CNC machining. In all cases, the spraying was performed using the Impact cold spray gun 5/8 equipped with the tungsten carbide de Laval nozzle Out1 (Impact innovations, DE).

An extensive literature review was done on the CS of S316L to set the optimum spraying parameters for the experimental campaign [3,28–39]. Based on previous parameter optimizations found in the literature and the limitations of the employed CS system, the baseline process parameters were set as reported in Table 2.

2.2.2. Initial characterization tests and equipment

The first set of experiments, carried out to obtain the input data for the shape prediction model, consists of 13 single-track depositions on rectangular ($25 \times 16\ mm^2$) samples with different secondary parameters reported in Table 3.

Each sprayed sample was englobed and polished. After sufficient polishing of the surfaces, the deposit profiles were photographed in slices with an optical microscope. The images were stitched together to form a continuous photo of the deposit profile. The composite images were then processed using the program, ImageJ [40]. First the composite images were transformed to grayscale, as displayed in Fig. 3(b). Then their pixel/length ratio was calculated, and finally the profile points, which were extracted by a MATLAB code, were transformed into coordinates, the result of which is the black profile shown in Fig. 3(c). The digitized profiles were analyzed to calculate different parameters of the constituent equations of the deposit growth model. Fig. 3(a) represents a composite image of deposit profile for the parameter set number 10.

After acquiring the deposit profile for all the samples and considering the prescribed general forms of the constituent equations, a MATLAB code was employed to calculate the fitting parameters, minimizing the RMSE of the experimental and the fitted profiles difference. The calculated model parameters are reported in Table 4.

The DE for each parameter set was calculated as the ratio of the weight of deposited powder to the weight of the sprayed powder while nozzle traveled over each sample. To further establish the pragmatic aspects of the approach, porosity of the obtained deposits was measured through analysis of the SEM micrograph images (with an example presented in Fig. 4) of each series. The average values for measured porosity of specific samples are reported in the results section to reflect the effect of nozzle travel speed, stand-off distance, and impact angle.

To validate the developed code, it was implemented for simulating the deposit profile for three distinct reference cases. These three cases, which are fully explained in [22], are designed to evaluate specific aspects of the code's capabilities, including the effect of spraying angle, effect of substrate's geometry, and shadow effect. In all three validation cases, the general form of the experimental and numerical profiles was in very good agreement. Furthermore, the model successfully appreciated the target aspect of each benchmark case. However, a slight overestimation of the deposit height was perceivable in all three validation cases, which as discussed in future sections if not checked, may lead to an exacerbated deviation from the experimental results in cases with higher number of passes.

It should be noted that the code works based on the polynomial equations that are fitted to the experimental deposit profiles. As the input parameters of the predictive model are taken from these polynomial curves and the building blocks of the code for deposit profile are also smooth polynomials, it cannot appreciate the local non-smooth nature of the deposits.

2.2.3. Repair and welding experiments

Three sets of experiments were conducted: 1) repair of various configurations of cut-through slots, 2) repair of enclosed cavities with varying geometries, and 3) welding of different butt-joint arrangements.

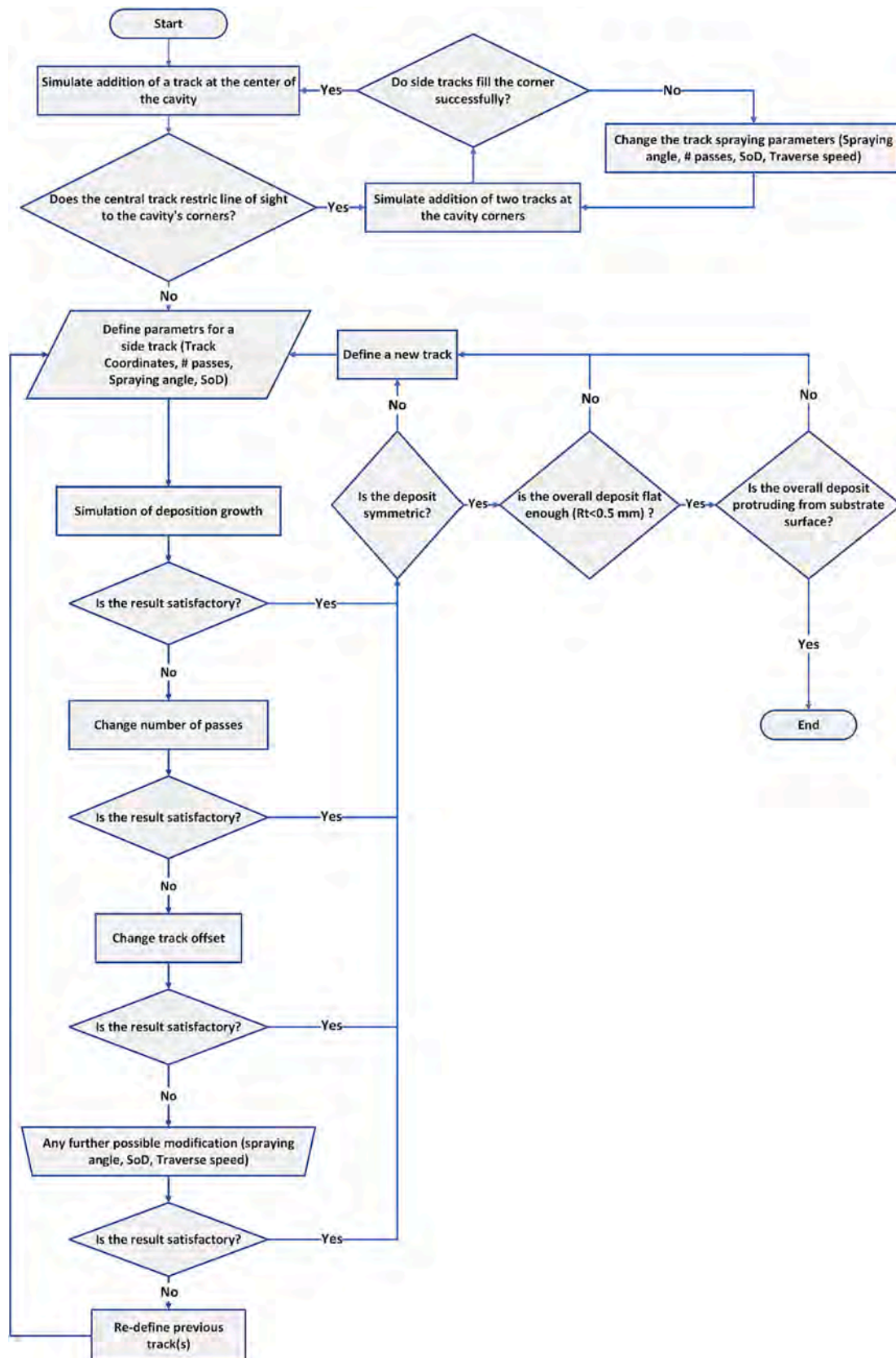In real cases, the initial geometry of the damage zone is usually

Fig. 1. The iterative algorithm for definition of the optimized toolpath strategy.

Table 1

Nominal chemical composition (wt%) of 316L stainless steel for substrate and powder [27].

Element	C	Ni	Cr	Mn	P	S	Si	Mo	N
wt%	0.020	11.21	17.38	1.860	0.027	0.0054	0.510	2.360	0.038
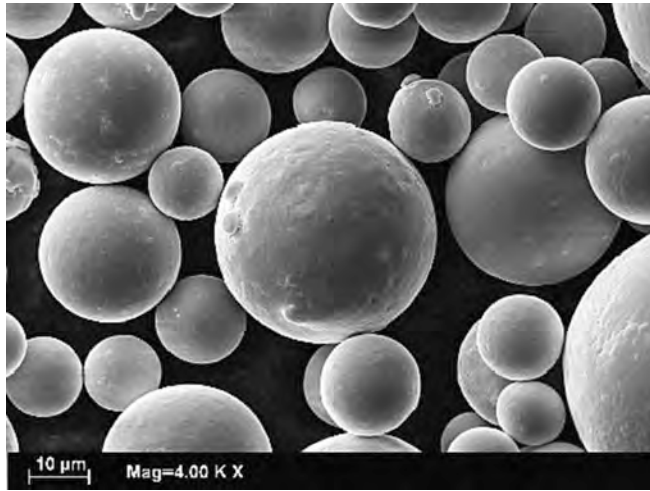
Fig. 2. SEM micrographs of the spherical S316L powder.

Table 2

Cold spray system parameters.

Gas type	T_G (°C)	P_G (bar)	Powder feed rate g/*min*	Nozzle traverse speed (mm/s)	Stand-off distance (mm)
N2	700	35	20	250	30

Table 3

Spraying parameters used for characterization tests.

Sample number	Sample length [mm]	Nozzle traverse speed [mm/s]	d_s [mm]	Number of passes	Impact angle [°]
1	15.2	250	30	20	90
2	15.3	150	30	20	90
3	15.0	350	30	20	90
4	15.3	250	30	20	80
5	15.1	250	30	20	70
6	15.1	250	30	20	60
7	15.1	250	30	20	50
8	14.9	250	30	10	90
9	14.9	250	30	14	90
10	14.9	250	25	20	90
11	15.1	250	35	20	90
12	14.8	250	40	20	90
13	15.0	250	45	20	90

Fig. 3. Composite cross-section image of the profile of characterization deposit number 10.

Table 4

Calculated parameters for fitted constituent equations.

	A	r_n	K_2
$A.J(r)$ parameters	2.2	4	0.9

	$tan(\alpha_n)$		k
$DE(\alpha)$	3.098		7.61

	a_0	a_1	a_2	a_3	a_4
DE(Standoff)	−4.415	0.6542	−0.02953	0.00059	− 4.4E − 6

modified and machined to a more regular shape, which is suitable for repair. In the case of CS repair, this defect bed preparation is necessary to assure that all the regions of target volume are accessible by the powder jet, a practical minimum DE is achievable on all target surfaces promoting the deposition of a uniform coating, which prompts a homogeneous and seamless integration with the original part. In addition, previous studies from our research group on the effect of cavity geometry on the quality of CS deposit, were consulted for selection of representative cavities [41], described schematically in Fig. 5 and Table 5.

It is worth reminding that the simulated scanning strategies consist of deposit tracks parallel to the longitudinal direction of the cavity.
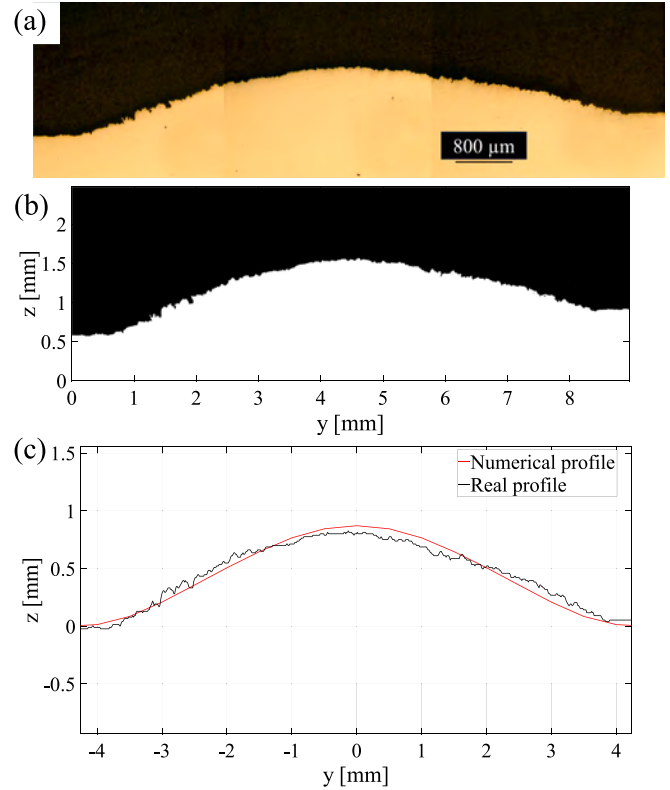
Furthermore, while nozzle's track can be modified to avoid over spraying on the far edges of the enclosed cavities, this was not a point of focus during this study.

Cut-through slots were studied to initially eliminate the boundary effect of the closed ends of the enclosed cavities and to provide a more accurate representation of the resultant simulated deposit profile. Two profiles with similar depth of 1.5 mm and width of 16 mm were considered for the cut-through samples: one with a 5r curved edge and the other with a 30° slope, as demonstrated in Fig. 5.

Five configurations of enclosed cavities were selected to evaluate the effect of edge shape, as well as the isolated effect of depth and width size, with their dimensions reported in Table 5.
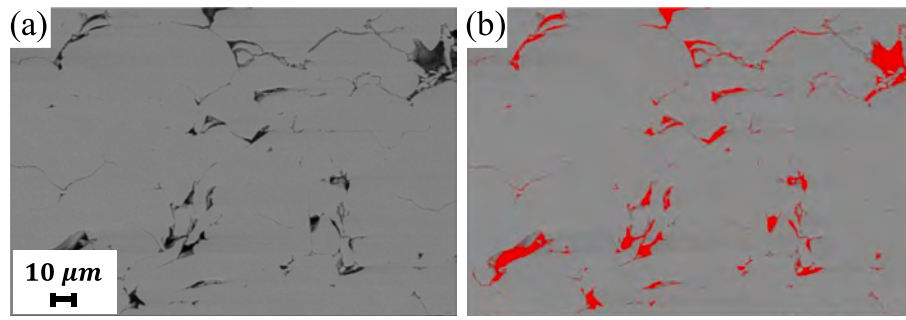
Fig. 4. Processing of SEM images for measurement of deposit porosity.
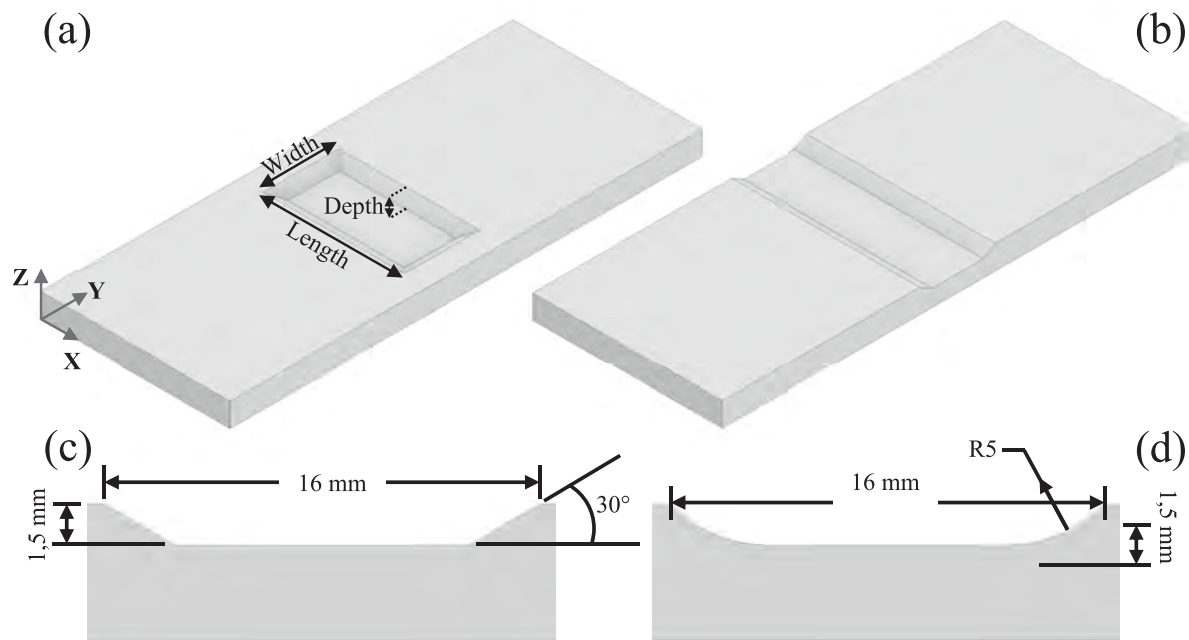

Fig. 5. Definition of geometric aspects of considered (a) enclosed and (b) cut-through cavities, and dimensions of cut-through slots with (c) 30° sloped edge and (d) 5 mm radius curved edge.

Table 5
Selected configurations for samples with enclosed cavities.

	16	16	32	Width (mm)
	1.5	2.5	1.5	Depth (mm)
Curved R5	✓	✓	✓	
Sloped 30°	✓			
Sloped 45°	✓			

The butt joint geometries employed for the analysis of CS welding were selected from the most conventional arrangements, with the condition that CS deposition constraints will allow for a complete and homogeneous deposition at the weld root. The first constraint was the target maximum deposit thickness of 5 mm to be achieved, which was selected as an achievable thickness with reference to previous studies on the application of CS as an AM method [3,42]. The second point that led to discarding some configurations such as K-shape or double-J shape, was the requirement for an acceptable deposition efficiency and compatibility with system's line of sight for all the weld faces. Another constraint was the necessity of accurate alignment of weld butts at the root, and a tight tolerance for the zero root gap during the CS, that is necessary for fabrication of a strong integrated weld. In specific configurations such as V+ or similar geometries, the interface at the root consists of two very thin edges, which are challenging to align and keep together while exposed to the high pressure of CS process gas. This led to discarding V+ and similar geometries. Therefore, the V-shape butt welds with 20° and 30° face angles were selected for the analysis. Weld-face slope angles were selected to accommodate a wide and simultaneously deep enough groove for placement of at least two deposit tracks of 8 mm width. The selected geometries are presented in Fig. 6.

While the focus of this paper is on optimization of CS toolpath strategy for achieving a satisfactory final deposit profile through predicting the geometrical evolution of the deposit, it is worth reminding that future research should also include a thorough evaluation of the final mechanical properties of the realized CS deposits. To address this concern, while remaining within the determined framework of this paper, results of preliminary measurements for microhardness and tensile strength of the created deposits are briefly discussed in the following section.

3. Results and discussion

The porosity of characterization samples with different process parameters are compared to choose the optimum set of process parameters for the other cases. The deposit profiles acquired from the experiments
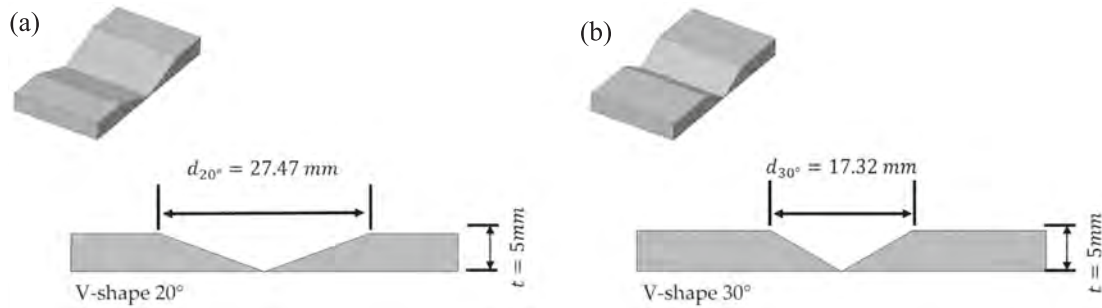
Fig. 6. Final geometries selected for the welding experiment.

and those simulated by the developed model are presented and compared in this section. In all cases, certain deviations of deposition parameters from those prescribed, and the fundamental assumptions of the numerical model are discussed for evaluating the capabilities of the presented model.

3.1. Measured porosity

Deposit porosity of eight characterization samples was measured by analyzing their cross-section SEM images with the help of ImageJ software [40]. The analyzed samples were selected to reflect the effect of variation of three process parameters in isolation, namely Nozzle traverse speed, stand-off distance, and impact angle. The measured porosity values are reported in Table 6.

Comparing the porosity for samples 1–3 it can be inferred that increase of nozzle traverse speed results in an overall increase of porosity. While the trend is not a steady decline, the variation of porosity with traverse speed is in line with the other experimental results reported in the literature [43]. The same observation can be made for the increase of deposit porosity with increase of stand-off distance, observed in samples 1, 11, and 13 [44]. An increased number of tests with wider range and smaller increments of process parameters can more clearly demonstrate their effect on porosity. It should be noted that, as also reported in the literature [44–46], the optimal process parameter is not always the lowest value and it may be indicated by the dip in porosity as well as deposition efficiency. On the other hand, the detrimental effect of smaller impact angle on the porosity is more evident through comparison of samples 1 and 5–7.

Based on the measured porosity, deposition efficiency, and the deposit profile of the 13 characterization samples, the process parameters presented in Table 2 were implemented for the spraying of the repair and welding samples.

3.2. Repair of cut through slots

For each case, the optimal deposition strategy was identified and simulated by following the proposed process indicated in flowchart of Fig. 1, with an example presented in Fig. 7. After spraying the cut-through samples with the optimized toolpaths, they were cut across the central transverse plane and the deposit profiles were extracted through microscopy observations. Comparison of the simulated and real profiles for the sample with cut-through slot with curved edges, as
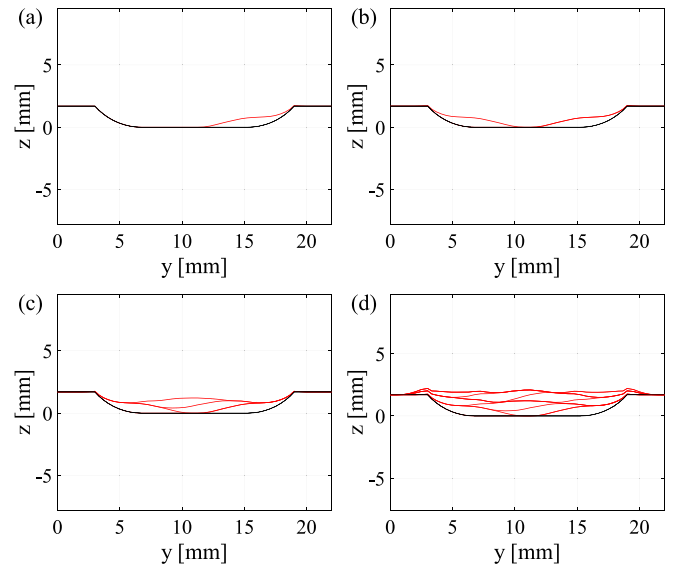

Fig. 7. Progressive view of deposition strategy for a cut-through slot of $1.5 \times 16 \text{ mm}^2$ after (a) 1, (b) 2, (c) 4, (d) and 10 steps.

shown in Fig. 8(a), indicates that while predicted profile closely describes the shape of the achieved profile, the overall height of experimentally obtained deposit is less than the one predicted by the model.

This can be interpreted as an overestimated DE by the model that can be attributed to uncertainties in fittings performed to define the input parameters. The input parameters for the numerical model are in all cases evaluated for depositions with a maximum of 20 passes on the same track. However, optimized repair deposition toolpaths rely on deposition of a higher number of passes. There might be a turning point after which the DE diminishes, as it is reported in the case of CS, since the shape of the deposit evolved and thus the angle of impact and consequently the local DE can be reduced as the number of passes increase. Another contributing factor may be the geometry of the cavity and how it diverges from the flat substrates, which were used in the characterization. The raised side edges of the cavity may result in a distinct disturbance of the impinging gas flow or may enforce the rebounding flow, and subsequently decrease the DE.

Table 6
Measured porosity for characterization samples.

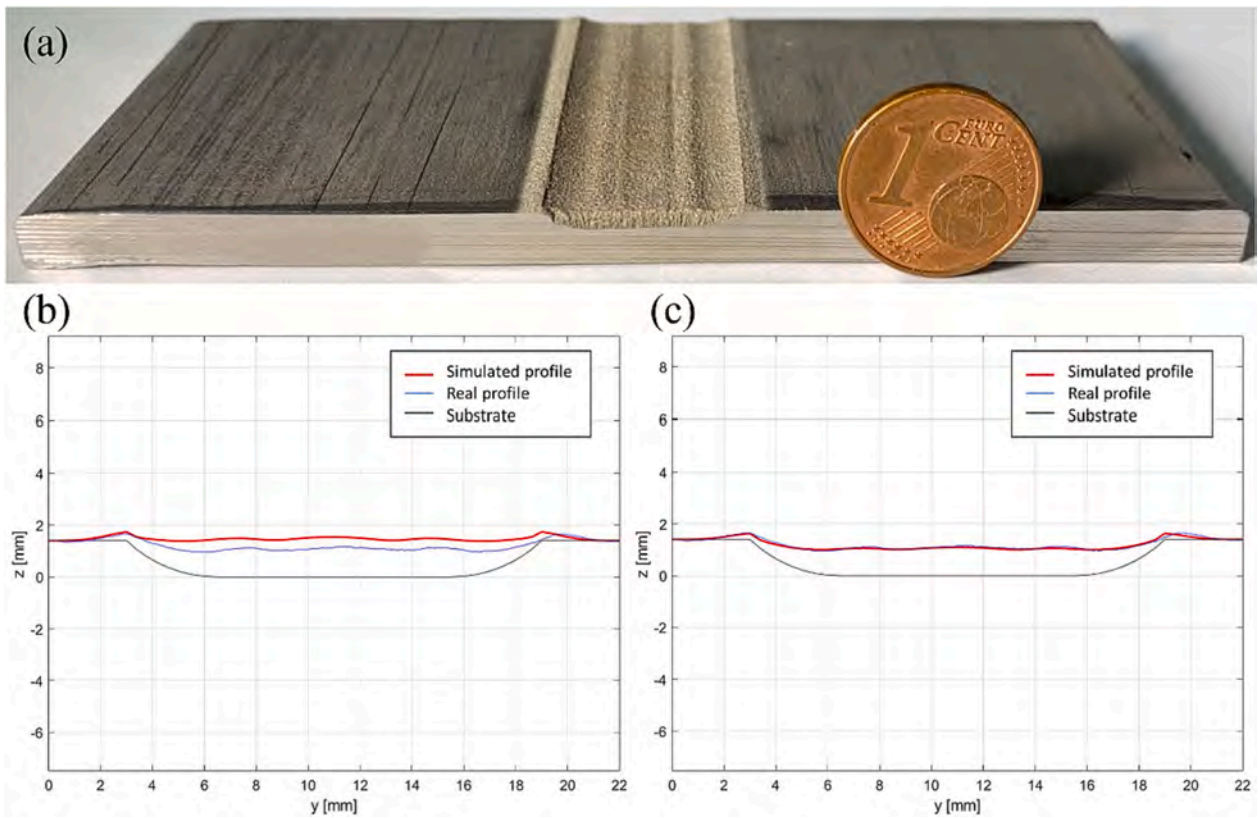| Sample no.	1	2	3	5	6	7	11	13
Speed (mm/s)	250	150	350	250	250	250	250	250
Impact angle (°)	90	90	90	70	60	50	90	90
SoD (mm)	30	30	30	30	30	30	35	45
Porosity (%)	0.793	0.609	0.668	1.557	3.914	1.345	0.643	2.775
SD	0.0141	0.0556	0.0589	0.5510	0.5789	0	0.0598	0.3455

Fig. 8. Comparison of deposit profiles for the 5r curved edge cut-through slot (a) from experimental results, and simulation (b) before and (c) after modification.

To solve this discrepancy a corrective coefficient (DEC) was considered, equal to the ratio of average deposit height across the width of the slot for the experimentally obtained deposit to that of the simulated deposit. The simulation for both curved and sloped edges was repeated implementing the DEC calculated as 0.71 in case of the cut-through slot with curved edges. As can be seen in Fig. 8(b), consideration of the DEC resulted in a significantly closer prediction of the observed deposit profile.

Fig. 9(a) demonstrates the comparison between the acquired and simulated deposit profiles for the slot with 30° sloped edges after applying the DEC. However, despite the well predicted average deposit height, some local peaks can be identified in the experimental results that cause local deviation between the predicted and the real profiles.

Fig. 9. Comparison of deposit profiles for the cut-through slot with 30° sloped edges (a) from experimental results, and simulation (b) without and (c) with consideration of machining traces.

A careful inspection of the manufactured slot before deposition reveals that placement and overall geometry of the peaks is a close projection the traces left after machining the bottom surface of the defect bed, which may be the reason for unexpected local deviations from the simulated profile. To assess this theory, small equilateral peaks were added to the substrate profile in the simulation. As confirmed by the results presented in Fig. 9(b), the simulated profile shows better conformity with the experimental data, proving that the local artifacts in the substrate's surface will be projected in the deposit's profile throughout the deposition process and will be eventually reflected on the top surface.

3.3. Repair of enclosed cavities

The next series of experiments included repairing the local enclosed cavities represented by the five selected geometries described in Fig. 5 and Table 5. The simulation results revealed that except in the case of deeper cavities, there is no benefit to spraying with inclined gun. Therefore, in cases with shallow cavities, the optimized toolpaths consist only of parallel tracks connected at the end through perpendicular motions along cavity's width.

As an example, the optimized toolpath strategy for the first sample with smallest cavity of 16×1.5 mm^2 with 5r curved edges is presented in Table 7 with an overview of the resultant deposit in Fig. 10. The toolpath strategy is presented in terms of placement of tracks, which is described by expressing the lateral distance between the track and center of cavity Δy (mm) and the number of passes along each track.

Comparing the profiles in the mid-section of the deposit with the simulated profile, presented in Fig. 11 reveals that the acquired deposit height is still slightly lower than the simulated profile. Therefore, following the same procedure as explained in Section 3.2, a DEC equal to 0.6 was calculated for this case. The further decrease in DE is proposed to be attributed to the more constrictive effect of fully enclosed cavity, as
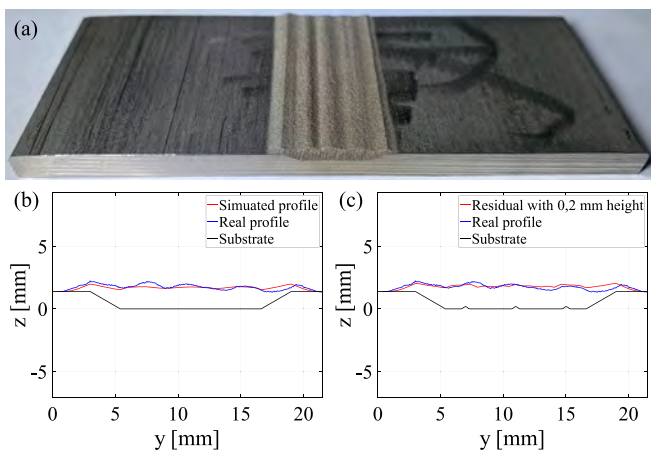
Table 7

Toolpath strategy for the 16 × 1.5 cavity with 5r curved edges.

	Track number									
	1	2	3	4	5	6	7	8	9	10
Number of passes	16	16	16	16	16	16	22	22	16	16
Δy (mm)	4.6	−4.6	−1.2	1.2	6	−6	−2	2	6	−6

Fig. 10. Overview of the 1.5 × 16 mm² cavity before and after spraying, (a) a combined view of the CAD design and actual machined cavity with the optimized toolpath strategy according to Table 7 overlayed, (b) the damage cavity after CS spraying with the proposed toolpath strategy.
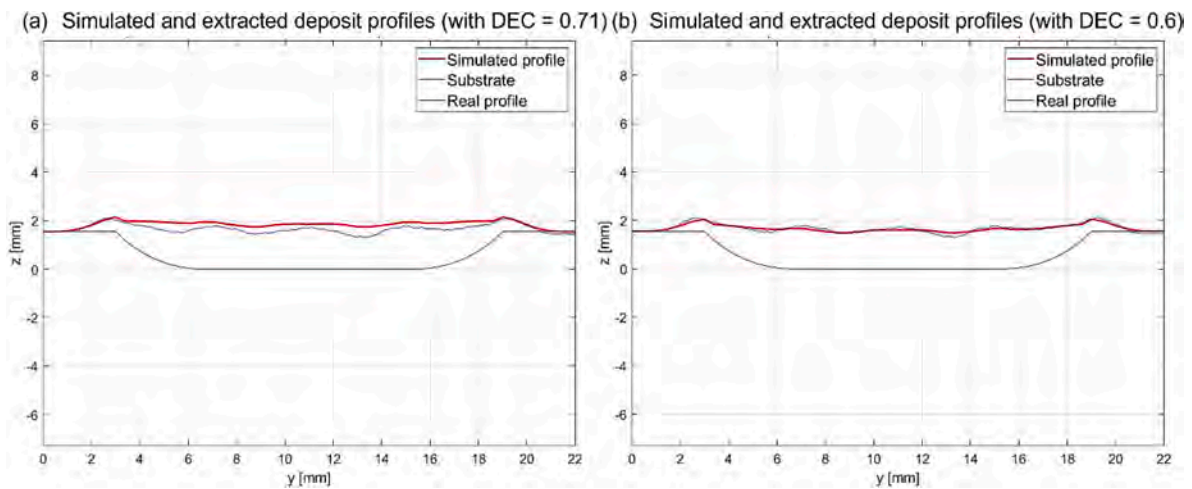
Fig. 11. Comparison of deposit profiles for the 1.5 × 16 mm² enclosed cavity with 5r curved edges with different DECs.

well its small aspect ratio on the carrier gas flow.

Also in this case, some local deviations from the smoother predicted profile were observed in the extracted profile in Fig. 11(a), which closely follow the machining marks present on the bottom and edges of the cavity (see Fig. 10).

The same process was followed for the other sample with enclosed but deeper cavity, with the only difference that deeper cavities required spraying some of the tracks with the nozzle inclined to efficiently fill the corners and make a more suitable bed for the subsequent layers. This contrasts with the cases for shallow cavities where the nozzle was always at 90° with respect to the cavity's bottom surface. The toolpath strategy for repair of the 2.5 × 16 mm² cavity with 5r curved edges is presented in Table 8. Here a row is added to describe the deviation of nozzle's

inclination from the usual 90° ($\Delta\alpha$).

It should be noted that employing a similar DEC as that of the 1.5 × 16 mm² cavity with 5r curved edges, a good agreement between the profiles is observed, as in Fig. 12. However, there are still some local discrepancies as well as a more pronounced asymmetry in the experimental profile.

The first reason for this deviation is the minor variation of gas pressure and temperature during spraying of initial inclined tracks. The inclination of nozzle results in variation, a decline during first track and increase during second track of gas pressure and temperature. Therefor during spraying the first two tracks, the parameters are not at the optimized level, leading to a lower DE than predicted. The other reason is slight misalignment of the nozzle's initial position with respect to the cavity, which results in an overall offset of the experimental deposit profile with respect to the cavity.

However, considering the good agreement of the obtained and simulated results with a DEC the same as that of a cavity of 1.5 mm depth, one can suggest that the depth variation (at least in the range considered in this study) does not significantly affect the DE.

The last repair sample to discuss has a 1.5 × 32 mm² cavity with 5r curved edges. The optimization process revealed that the efficient repair of this cavity, like other shallow cavities, does not require inclined spraying. In addition, applying a new calculated DEC equal 0.85 results
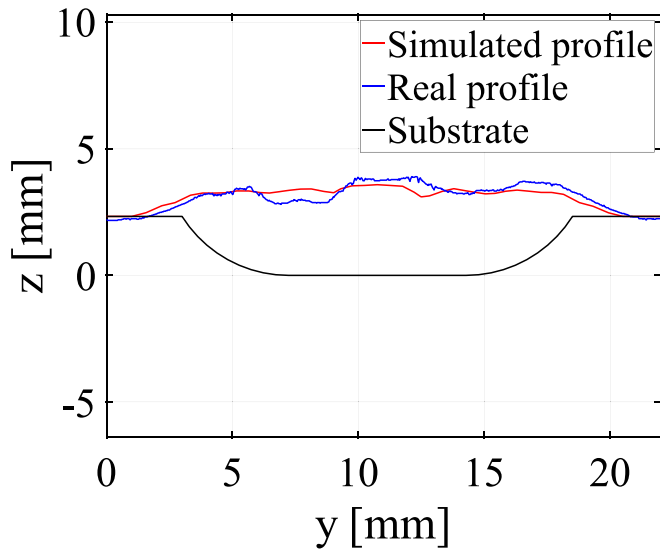
Table 8

Toolpath strategy for first six tracks for the 1.5 × 16 mm cavity with 5r curved edges.

	Track number					
	1	2	3	4	5	6
Number of passes	26	26	22	22	22	22
Δy (mm)	6	−6	−3.5	3.5	1	−1
$\Delta\alpha$	30°	−30°	0	0	0	0

Fig. 12. Comparison of deposit profiles for the 2.5×16 mm^2 enclosed cavity with 5r curved edges.

in a satisfying profile prediction, as is evident in Fig. 13.

Even though the collected data may not be conclusive, the results indicate that if the cavity's aspect ratio is defined as the ratio of its length to its width, a relation between cavity's aspect ratio and the DEC can be proposed. It is proposed that for aspect ratios close to zero (very wide cavities) the DEC approaches a value of 1, and it may decrease in a non-linear manner with respect to increasing aspect ratio.

3.4. Welding of different butt joint arrangements

Optimization of toolpath strategy for the two selected butt-weld geometries started with investigating the deposit growth at the adjoining edge interface with varying numbers of passes. The deposit track covering this region is critical because it determines the quality of the final weld, especially since this track has the most complex substrate configuration among all other subsequent deposit tracks. As can be perceived from Fig. 14, this effect is less pronounced for the 20° notch

compared to the 30° notch geometry. Our preliminary analyses revealed that even with the relatively narrow notch and even with high number of passes, it is impossible to fill the notch completely with a single track.

To develop a realistic strategy, first, adding a track should contribute to increasing the flatness of the deposit. Hence, the lowest points on deposit surface would be the initial choices for addition of the next track. Second, the detrimental effect of edges on DE, and therefore slower deposit growth at these points should be considered. The final optimized toolpath strategies for 30° and 20° notches consisted of 270 and 384 passes, respectively. The toolpath strategy for filling the 30° notch is presented in Table 9 and the predicted deposit geometries for both configurations are presented in Fig. 15.

The slight asymmetry evident in deposit profiles, which is more pronounced for the 20° notch deposit, arises from the imperfect initial alignment of the adjoining edges of the two pieces of substrate, as well as misalignment of the nozzle's starting point and motion direction with respect to interface edges. Both factors can be further mitigated through implementation of a more accurate fixture and better calibration.

Also in this case, comparison of the obtained and predicted profiles revealed the necessity of implementing a corrective coefficient, which was found to be equal to 0.69. The lower value compared to the DEC determined for the repair cases may be due to the more constrictive geometry of the V-notch in comparison to that of the cavities. However, after applying this corrective factor a very good agreement between the predicted and experimentally obtained profiles was found, as can be observed in Fig. 16.

3.5. Mechanical characterization of the realized CS deposits

3.5.1. Microhardness measurements

The tamping effect of the progressively impacting particles will induce work hardening and an increase in the hardness of the deposited powders in comparison to that of the bulk material (i.e., in this case the substrate). This leads to the brittle behavior of the CS deposit in the as-sprayed state. In many cases, higher ductility is desirable, and various studies in the literature have proposed the necessity of performing a post-deposition heat treatment to recover the ductility and fracture toughness of the CS deposit [3,47–49]. Providing a preliminary analysis of microhardness variation across the deposit-substrate cross-section can highlight the necessity of post-processing for achieving satisfactory
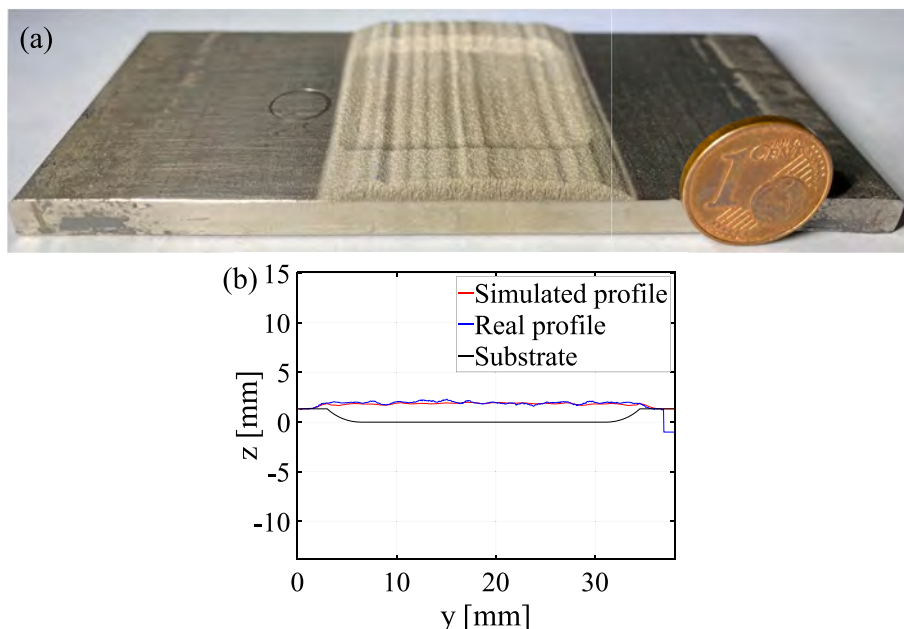

Fig. 13. (a) An overview of repaired enclosed cavity of 1.5×32 mm^2 and (b) comparison of achieved and simulated profiles.
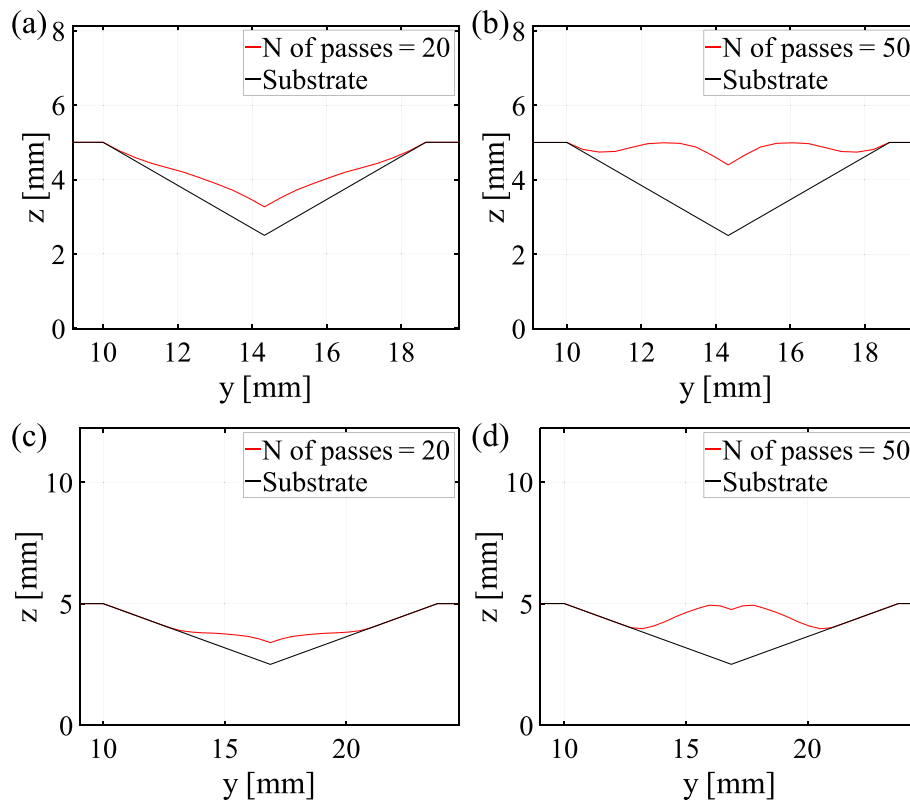
Fig. 14. Comparison of central track growth after (a) 20 and (b) 50 passes over 30° notch, and after (c) 20 and (d) 50 passes over 20° notch.

Table 9
Toolpath strategy for welding the 30° notch butt weld joint.

	Track number											
	1	2	3	4	5	6	7	8	9	10	11	12
Number of passes	40	20	20	40	20	20	30	20	20	20	10	10
Δy (mm)	0	−4	4	0	−4	4	0	−6	6	0	−4	4

mechanical properties.

To this end, a representative repair sample (the sample with enclosed cavity of 1.5×16 mm² with 5r curved edges) was cut orthogonal to the spraying tracks, englobed, and polished and then Vickers microhardness measurements were conducted on its cross-section at equidistant steps of 0.30 mm from the deposit's top surface, as indicated in the Fig. 17.

For the microhardness measurements a load of 300 gF was applied with a dwelling time of 20 s. Furthermore, the indentation points were positioned far enough from each other and the deposit's top surface and the deposit-substrate interface. The results clearly indicate the effect of work hardening on the hardness of the deposit and a clear decline of the hardness when passing from the deposit to the substrate.

The hardness was measured on the cross-section of the repair sample at five levels with the sixth measurement conducted on the substrate near the interface, each repeated three times. Table 10 summarizes the average values of the measured Vickers microhardness and the corresponding standard deviation. It should be noted that the microhardness distribution across a coating is not expected to be perfectly uniform and can be highly affected by the measurement position with respect to the splat boundaries and their size and deformation, among many other factors.

As can be seen, a significant decrease in the measured microhardness between the fifth and the sixth measurements is a clear indication of transfer from the deposit to the substrate. In addition, the considerably higher microhardness of the deposit (almost twice the microhardness of substrate), as expected, is a result of work-hardening of the CS deposited particles and considerable tamping effect of the consequently deposited layers.

3.5.2. Tensile strength of the CS deposited welds

To have a qualitative evaluation of the interface adhesion strength and the integrity of the weld, a tensile test was conducted on the welded parts with excess deposit machined down to a flat surface. The 20° V and 30° V notch samples failed at an average stress of around 5 MPa and 13 MPa, respectively, with the 30° V notch sample showing a significantly higher strength. In both cases the fracture initiation and growth occurred through the deposit and no delamination was observed. While the reported tensile strengths seem rather low for welding applications, this behavior at the tested state is expected. First, a literature review [3,50] reveals the necessity of various post-processes such as heat treatment to recover the ductility and decrease the porosity of the CS deposit. Furthermore, as stated in the reported observations, a more robust fixture should be designed and employed to hold the weld joint edges of the separate parts aligned throughout the CS process. In addition, the nozzle's initial calibration should be improved to enhance the alignment of the weld edges and the nozzle tracks. These adjustments improve the integrity and in turn mechanical properties of the CS weld, which can be explored in future studies.
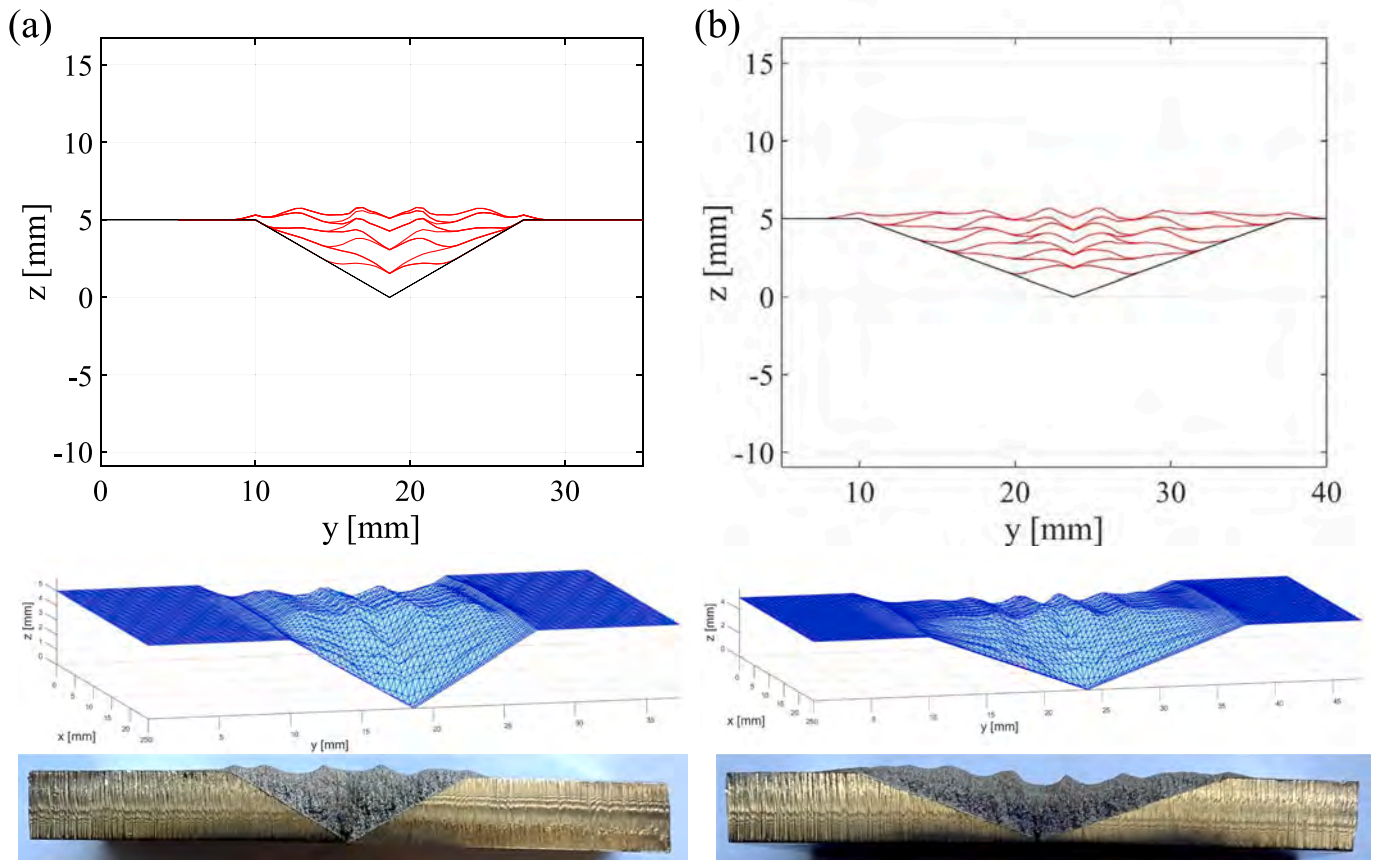
Fig. 15. Comparison of predicted progressive deposit growth and final deposit profile in 2D and 3D with the acquired profile for (a) 30° notch and (b) 20° notch.
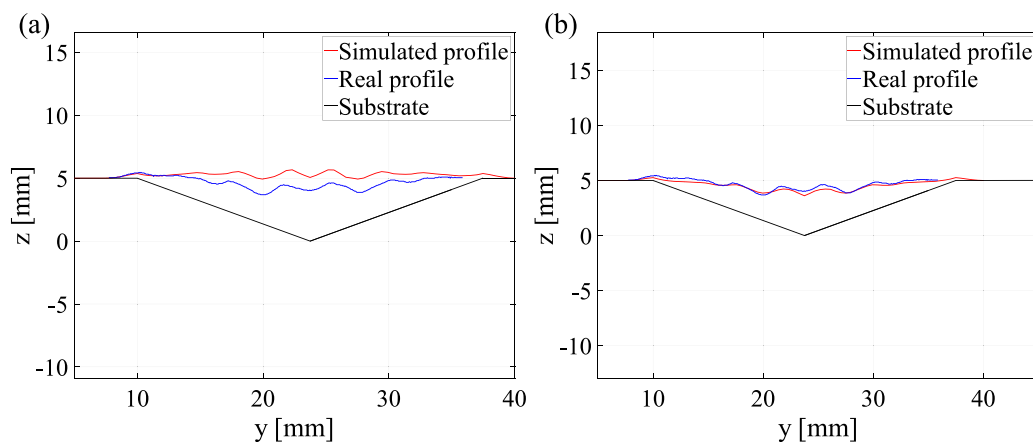

Fig. 16. Comparison of acquired and predicted deposit profile for 20° V notch weld (a) before and (b) after applying DEC.
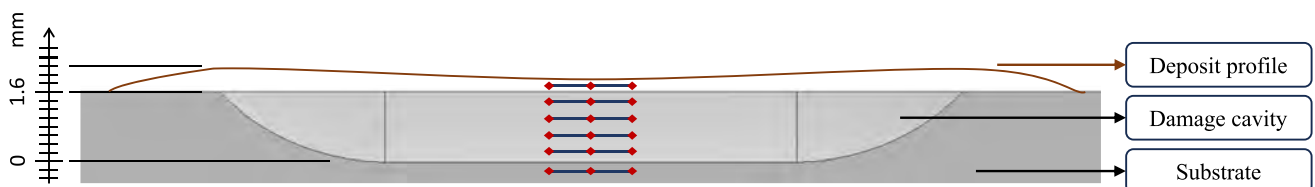

Fig. 17. Arrangement of microhardness measurement points across the cross section of the repaired sample.

Table 10
Vickers microhardness measurement results across the deposit cross-section.

Measurement #	Measurement height (μm)	HV
1	1400	351.3 ± 37.3
2	1050	274.4 ± 36.2
3	750	314.2 ± 69.5
4	450	332.7 ± 55.0
5	150	301.0 ± 25.4
6	-150	167.3 ± 5.7

4. Conclusions

Here a deposit shape prediction model, previously developed in our research group, was further enhanced by being integrated into an iterative scheme, which allows the optimization of toolpath strategy for efficiently filling different geometries of cavity with desired criteria. In this research two general applications, repair of different cavities and welding of two adjoining parts, were considered.

The developed numerical model can be successfully applied for different substrate geometries and powder-substrate material combinations. Here, the deposit shape prediction parameters for CS of 316 L steel powder on the substrate of the same material were determined from experimental results. The developed model together with the iterative scheme were used to optimize the arrangement of deposition tracks based on the target geometry. The qualitative optimization criteria were set as the relative deposit surface flatness and the minimum number of tracks necessary to protrude from the substrate flat surface. After accounting for some discrepancies in deposition efficiency, it was shown that in all cases the developed model can successfully predict the deposit profile shape with high accuracy.

Based on the findings it can be concluded that:

– It was demonstrated that a corrective coefficient, which is proposed to depend on geometrical aspects of the cavity, can be introduced to account for variation of deposition efficiency from the characterized value.
– This variation, which is proposed to be attributed to the disturbance of impinging gas flow on non-flat surfaces, is more pronounced in the welding cases with V-shaped butt welds.
– An accurate calibration of nozzle's motion with respect to the deposition target and implementation of a robust fixture for each application can further increase the consistency between the predicted and experimentally acquired deposit profiles.

Overall, the developed enhanced numerical model can successfully predict the cold sprayed deposit distribution and profile of any desired material over any arbitrary substrate geometry, provided that the required input parameters are calculated with high precision, and the experiments are accurately conducted.

Declaration of competing interest

The authors declare that they have no known competing financial interests or personal relationships that could have appeared to influence the work reported in this paper.
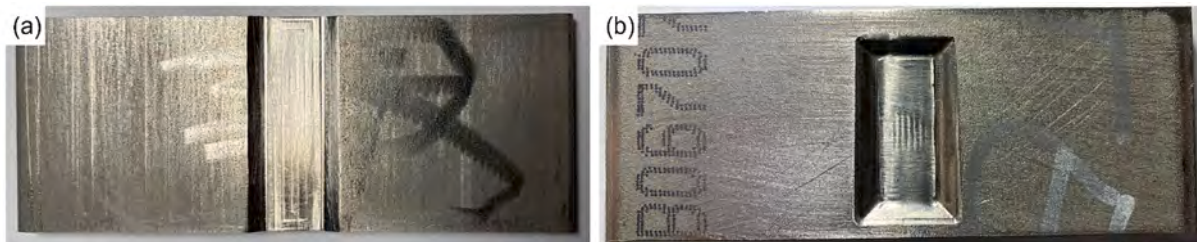
Appendix A. Additional figure

Fig. A1. A1 (a) The cut-through slot sample with 30° slope, (b) enclosed cavity pf 16 × 1.5 with 30° sloped edges.

References

[1] Kanishka K, Acherjee B. Revolutionizing manufacturing: a comprehensive overview of additive manufacturing processes, materials, developments, and challenges. J Manuf Process 2023;107:574–619. https://doi.org/10.1016/j.jmapro.2023.10.024.

[2] Vaezi M, Drescher P, Seitz H. Beamless metal additive manufacturing. Mater 2020;13:922. https://doi.org/10.3390/MA13040922.

[3] Bagherifard S, Kondas J, Monti S, Cizek J, Perego F, Kovarik O, et al. Tailoring cold spray additive manufacturing of steel 316 L for static and cyclic load-bearing applications. Mater Des 2021;203:109575. https://doi.org/10.1016/j.matdes.2021.109575.

[4] Bagherifard S, Heydari Astaraee A, Locati M, Nawaz A, Monti S, Kondás J, et al. Design and analysis of additive manufactured bimodal structures obtained by cold spray deposition. Addit Manuf 2020;33:101131. https://doi.org/10.1016/j.addma.2020.101131.

[5] Ardeshiri Lordejani A, Vitali L, Guagliano M, Bagherifard S. Estimating deposition efficiency and chemical composition variation along thickness for cold spraying of composite feedstocks. Surf Coat Technol 2022;436:128239. https://doi.org/10.1016/j.surfcoat.2022.128239.

[6] Bagherifard S, Monti S, Zuccoli MV, Riccio M, Kondás J, Guagliano M. Cold spray deposition for additive manufacturing of freeform structural components compared to selective laser melting. Mater Sci Eng A 2018;721:339–50. https://doi.org/10.1016/j.msea.2018.02.094.

[7] Mundra K, Blackburn JM, DebRoy T. Absorption and transport of hydrogen during gas metal arc welding of low alloy steel. Sci Technol Weld Join 1997;2:174–84. https://doi.org/10.1179/stw.1997.2.4.174.

[8] Gedeon SA, Eagar TW. Thermochemical analysis of hydrogen absorption in welding. Weld Res Suppl 1990:264–71. https://citeseerx.ist.psu.edu/document?repid=rep1&type=pdf&doi=0fa8f9fa34602eb99146d5910a06b156271326cc [accessed February 7, 2023].

[9] Srivastava B, Tewari S, Jyoti P. A review on effect of preheating and/or post weld heat treatment (PWHT) on mechanical behavior of ferrous metals. Citeseer 2010;2 (2010):625–31. http://citeseerx.ist.psu.edu/viewdoc/download?doi=10.1.1.188.8462&rep=rep1&type=pdf (accessed July 11, 2022).

[10] Moat RJ, Stone HJ, Shirzadi AA, Francis JA, Kundu S, Mark AF, et al. Design of weld fillers for mitigation of residual stresses in ferritic and austenitic steel welds. Sci Technol Weld Join 2011;16:279–84. https://doi.org/10.1179/1362171811Y.0000000003.

[11] Ferreira JM, Branco CM. Influence of fillet weld joint geometry on fatigue crack growth. Theor Appl Fract Mech 1991;15:131–42. https://doi.org/10.1016/0167-8442(91)90012-9.

[12] Aprilia A, Tan JL, Yang Y, Tan SC, Zhou W. Induction brazing for rapid localized repair of Inconel 718. Metals 2021;11:1096. https://doi.org/10.3390/MET11071096.

[13] Hoyingchareon K, Muangjunburee P. Welding repair of aluminium alloy 6082 T6 by TIG welding process. Mater Sci Forum 2016;872:3–7. https://doi.org/10.4028/WWW.SCIENTIFIC.NET/MSF.872.3.

[14] Korinko P, Adams T, Malene S, Gill D, Smugeresky J. Laser engineered net shaping® for repair and hydrogen compatibility. Weld J 2011;90(9):171s–81s. App.Aws.Org. https://app.aws.org/wj/supplement/wj201109_s171.pdf (accessed July 12, 2022).

[15] Liu D, Lippold JC, Li J, Rohklin SR, Vollbrecht J, Grylls R. Laser engineered net shape (LENS) technology for the repair of Ni-base superalloy turbine components. Metall Mater Trans A Phys Metall Mater Sci 2014;45:4454–69. https://doi.org/10.1007/s11661-014-2397-8.

[16] Marya M, Singh V, Hascoet JY, Marya S. A metallurgical investigation of the direct energy deposition surface repair of ferrous alloys. J Mater Eng Perform 2018;27:813–24. https://doi.org/10.1007/s11665-017-3117-5.

[17] Rittinghaus SK, Schmelzer J, Rackel MW, Hemes S, Vogelpoth A, Hecht U, et al. Direct energy deposition of TiAl for hybrid manufacturing and repair of turbine blades. Materials (Basel) 2020;13:1–14. https://doi.org/10.3390/ma13194392.

[18] Oh WJ, Lee WJ, Kim MS, Jeon JB, Shim DS. Repairing additive-manufactured 316L stainless steel using direct energy deposition. Opt Laser Technol 2019;117:6–17. https://doi.org/10.1016/j.optlastec.2019.04.012.

[19] Klinkov SV, Kosarev VF, Ryashin NS, Shikalov VS. Influence of particle impact angle on formation of profile of single coating track during cold spraying. In: AIP Conf. Proc. American Institute of Physics Inc.; 2018. p. 20012. https://doi.org/10.1063/1.5065085.

[20] Klinkov SV, Kosarev VF, Shikalov VS. Control of cold spray process by changing of nozzle setting angle. In: AIP Conf. Proc. American Institute of Physics Inc.; 2019. https://doi.org/10.1063/1.5117382.

[21] Wu H, Xie X, Liu M, Chen C, Liao H, Zhang Y, et al. A new approach to simulate coating thickness in cold spray. Surf Coat Technol 2020;382:125151. https://doi.org/10.1016/J.SURFCOAT.2019.125151.

[22] Vanerio D, Kondas J, Guagliano M, Bagherifard S. 3D modelling of the deposit profile in cold spray additive manufacturing. J Manuf Process 2021;67:521–34. https://doi.org/10.1016/j.jmapro.2021.05.013.

[23] Ikeuchi D, Vargas-Uscategui A, Wu X, King PC. Neural network modelling of track profile in cold spray additive manufacturing. Mater 2019;12:2827. https://doi.org/10.3390/MA12172827.

[24] Sadiku MNO, Obiozor CN. Simple introduction to the method of lines. Int J Electr Eng Educ 2000;37:282–96. https://doi.org/10.7227/IJEEE.37.3.8.

[25] Chandio M, Journal AM-SUR, U.. Improving the efficiency of Heun's method. In: Researchgate.Net; 2010. https://www.researchgate.net/profile/Abdul-Memon-15/publication/344461764_Improving_the_efficiency_of_Heun's_Method/links/5faf773192851cf24cce0f4a/Improving-the-efficiency-of-Heuns-Method.pdf (accessed February 20, 2023).

[26] Vanerio D. 3D simulation of cold spray deposit profile: towards digitalization of cold spray additive manufacturing. 2020.

[27] Mohammad KA, Syams Zainudin E, Salit S, Zahari I, Ali A. Experimental determination of the fatigue behavior of austenitic 316L stainless steel under fatigue and creep-fatigue tests at high temperature. Int J Met Steel Res Technol 2013;1:1–11. https://www.researchgate.net/profile/Aidy-Ali/publication/284698427_Experimental_determination_of_the_fatigue_behavior_of_austenitic_316L_stainless_steel_under_fatigue_and_creep-fatigue_tests_at_high_temperature/links/573d299f08ae298602e59cc3/Experimental [accessed December 19, 2022].

[28] Adachi S, Ueda N. Effect of cold-spray conditions using a nitrogen propellant gas on AISI 316L stainless steel-coating microstructures. Coatings 2017;7. https://doi.org/10.3390/coatings7070087.

[29] Xie Y, Planche MP, Raoelison R, Liao H, Suo X, Hervé P. Effect of substrate preheating on adhesive strength of SS 316L cold spray coatings. J Therm Spray Technol 2016;25:123–30. https://doi.org/10.1007/s11666-015-0312-5.

[30] Radhamani AV, Lau HC, Ramakrishna S. 316L stainless steel microstructural, mechanical, and corrosion behavior: a comparison between spark plasma sintering, laser metal deposition, and cold spray. J Mater Eng Perform 2021;30:3492–501. https://doi.org/10.1007/s11665-021-05571-0.

[31] Fukanuma H, Ohno N, Sun B, Huang R. In-flight particle velocity measurements with DPV-2000 in cold spray. Surf Coat Technol 2006;201:1935–41. https://doi.org/10.1016/j.surfcoat.2006.04.035.

[32] Al-Mangour B, Vo P, Mongrain R, Irissou E, Yue S. Effect of heat treatment on the microstructure and mechanical properties of stainless steel 316L coatings produced by cold spray for biomedical applications. J Therm Spray Technol 2014;23:641–52. https://doi.org/10.1007/s11666-013-0053-2.

[33] Yin S, Cizek J, Yan X, Lupoi R. Annealing strategies for enhancing mechanical properties of additively manufactured 316L stainless steel deposited by cold spray. Surf Coat Technol 2019;370:353–61. https://doi.org/10.1016/j.surfcoat.2019.04.012.

[34] Borchers C, Schmidt T, Gärtner F, Kreye H. High strain rate deformation microstructures of stainless steel 316L by cold spraying and explosive powder compaction. Appl Phys A Mater Sci Process 2008;90:517–26. https://doi.org/10.1007/s00339-007-4314-0.

[35] Sova A, Grigoriev S, Okunkova A, Smurov I. Cold spray deposition of 316L stainless steel coatings on aluminium surface with following laser post-treatment. Surf Coat Technol 2013;235:283–9. https://doi.org/10.1016/j.surfcoat.2013.07.052.

[36] Yin S, Jenkins R, Kazasidis M, Lupol R, Yan X, Chen C. Hybrid additive manufacture of 316L stainless steel with cold spray and selective laser melting: microstructure, mechanical properties and case study. In: Proc. int. therm. spray conf.; 2019. p. 802–9. https://www.sciencedirect.com/science/article/pii/S0924013619302122 (accessed December 22, 2022).

[37] Al-Mangour B, Mongrain R, Irissou E, Yue S. Improving the strength and corrosion resistance of 316L stainless steel for biomedical applications using cold spray. Surf Coat Technol 2013;216:297–307. https://doi.org/10.1016/j.surfcoat.2012.11.061.

[38] Kotoban D, Grigoriev S, Okunkova A, Sova A. Influence of a shape of single track on deposition efficiency of 316L stainless steel powder in cold spray. Surf Coat Technol 2017;309:951–8. https://doi.org/10.1016/j.surfcoat.2016.10.052.

[39] Li WY, Liao H, Douchy G, Coddet C. Optimal design of a cold spray nozzle by numerical analysis of particle velocity and experimental validation with 316L stainless steel powder. Mater Des 2007;28:2129–37. https://doi.org/10.1016/j.matdes.2006.05.016.

[40] Rasband, W.S., Image J, U.S. National Institutes of Health, Bethesda, Maryland, USA, imagej.nih.gov/ij/, 1997–2011.

[41] Petráčková K, Kondás J, Guagliano M. Fixing a hole (with cold spray). Int J Fatigue 2018;110:144–52. https://doi.org/10.1016/j.ijfatigue.2018.01.014.

[42] Yin S, Cavaliere P, Aldwell B, Jenkins R, Liao H, Li W, et al. Cold spray additive manufacturing and repair: fundamentals and applications. Addit Manuf 2018;21:628–50. https://doi.org/10.1016/j.addma.2018.04.017.

[43] Seraj RA, Abdollah-zadeh A, Dosta S, Canales H, Assadi H, Cano IG. The effect of traverse speed on deposition efficiency of cold sprayed Stellite 21. Surf Coat Technol 2019;366:24–34. https://doi.org/10.1016/j.surfcoat.2019.03.012.

[44] Zahiri SH, Antonio CI, Jahedi M. Elimination of porosity in directly fabricated titanium via cold gas dynamic spraying. J Mater Process Technol 2009;209:922–9. https://doi.org/10.1016/j.jmatprotec.2008.03.005.

[45] Li WY, Zhang C, Guo XP, Zhang G, Liao HL, Li CJ, et al. Effect of standoff distance on coating deposition characteristics in cold spraying. Mater Des 2008;29:297–304. https://doi.org/10.1016/J.MATDES.2007.02.005.

[46] Mohankumar A, Duraisamy T, Sampathkumar D, Ranganathan S, Balachandran G, Kaliyamoorthy M, et al. Optimization of cold spray process inputs to minimize porosity and maximize hardness of metal matrix composite coatings on AZ31B magnesium alloy. J Nanomater 2022;2022. https://doi.org/10.1155/2022/7900150.

[47] Zhang Y, Qin B, Chan KC, Lupoi R, Yin S, Xie Y, et al. Enhancement on mechanical properties of CoCrNi medium entropy alloy via cold spray additive manufacturing associated with sintering. J Manuf Process 2023;94:413–23. https://doi.org/10.1016/j.jmapro.2023.03.017.

[48] Cortés R, Garrido MA, Rico A, Múnez CJ, Poza P, Martos AM, et al. Effect of processing conditions on the mechanical performance of stainless steel cold sprayed coatings. Surf Coat Technol. 2020;394:125874. https://doi.org/10.1016/j.surfcoat.2020.125874.

[49] Lomo FN, Vargas-Uscategui A, King PC, Patel MJ, Cole IS. Microstructure and mechanical properties of heat-treated cold spray additively manufactured titanium metal matrix composites. J Manuf Process 2023;99:12–26. https://doi.org/10.1016/j.jmapro.2023.04.077.

[50] Yin S, Cavaliere P, Aldwell B, Jenkins R, Liao H, Li W, et al. Cold spray additive manufacturing and repair: fundamentals and applications. Addit Manuf 2018;21:628–50. https://doi.org/10.1016/j.addma.2018.04.017.